Ten-percent solar-to-fuel conversion with nonprecious materials

Casandra R. Cox[a,1], Jungwoo Z. Lee[b], Daniel G. Nocera[a,1], and Tonio Buonassisi[b,1]

[a]Department of Chemistry and Chemical Biology, Harvard University, Cambridge, MA 02138; and [b]Department of Mechanical Engineering, Massachusetts Institute of Technology, Cambridge, MA 02139

Contributed by Daniel G. Nocera, August 1, 2014 (sent for review July 4, 2014)

Direct solar-to-fuels conversion can be achieved by coupling a photovoltaic device with water-splitting catalysts. We demonstrate that a solar-to-fuels efficiency (SFE) > 10% can be achieved with nonprecious, low-cost, and commercially ready materials. We present a systems design of a modular photovoltaic (PV)–electrochemical device comprising a crystalline silicon PV minimodule and low-cost hydrogen-evolution reaction and oxygen-evolution reaction catalysts, without power electronics. This approach allows for facile optimization en route to addressing lower-cost devices relying on crystalline silicon at high SFEs for direct solar-to-fuels conversion.

solar cell | earth abundant | renewable | artificial leaf | multijunction

Distributed and grid-scale adoption of nondispatchable, intermittent, renewable-energy sources requires new technologies that simultaneously address energy conversion and storage challenges (1, 2). Coupling photovoltaics to drive catalytic fuel-forming reaction, such as water splitting to generate H_2, allows for direct solar-to-fuels conversion. The solar-generated H_2 can effectively be harnessed to electricity by fuel cell devices (3, 4) or converted to liquid fuels upon its combination with CO or CO_2 (5–7). For this technology to be effectively implemented, a solar-to-fuels conversion efficiency (SFE) of 10% or higher is desirable (8, 9).

Direct photoelectrochemical (PEC) water splitting by a single absorber material has attracted a vast amount of attention (10, 11), and recent progress indicates improvements in the field (12, 13); but after decades of research, direct PEC faces three challenges to increase conversion efficiency: (*i*) Direct absorber band alignment is required to provide carriers with appropriate potential to both half reactions. Although such an alignment is difficult to achieve in a single material initially, any change in band alignment due to changing surface conditions can result in further efficiency degradation. This makes it challenging to design devices that maintain robust, high efficiencies in actual operation. (*ii*) The wide absorber bandgap (>1.23 eV; typically >1.6 eV) needed to drive the water-splitting reaction is not optimized for the solar spectrum, which results in a maximum SFE of only 7% (14–16). (*iii*) The absorbers are poor catalysts, and they are incapable of efficiently performing the four proton-coupled electron transfer chemistry (17–22) that is needed for water splitting.

These deficiencies can be overcome by substituting a PEC device with a buried-junction photovoltaic (PV) device and an electrochemical catalyst (EC) system, forming a PV–EC tandem (23–27). In a buried-junction device, the electric field is generated at an internal junction within the semiconductor and is then coupled with water-splitting catalysts through ohmic contacts, which can either be conductive coatings directly deposited onto the PV or connected through wires to the electrodes. The buried junction relaxes the constraints imposed by a PEC device because it separates light absorption from catalysis, and does not require that the absorber be stable in aqueous electrolytes in which the pH regime for the absorber and best water-splitting catalyst may not be compatible. However, PV–EC devices have been viewed historically as too expensive to be economically viable, primarily because of the use of noble-metal water-splitting catalysts and expensive and/or low-efficiency PV devices. Indeed, the solar splitting of water by nonprecious materials and under simple conditions has long been identified to be a "holy grail" of solar energy conversion (28). We have pursued this goal by using a buried-junction device coated with transparent conducting oxides, overlaid with self-healing catalysts that self-assemble upon oxidation of Co^{2+} (29–36), Ni^{2+} (37–39), and Mn^{2+} (40, 41) ions in phosphate or borate electrolytes. These catalysts have shown great fidelity for interfacing with a variety of buried junctions (42–46) to deliver what is more commonly known as the artificial leaf (47). This approach is generally being adopted by others (48, 49).

Efficiencies are predicted to be as high as 18% for PV–EC devices comprising series-connected single-junction PV devices and higher for multijunction PV devices (14–16). Of significant consequence to the design of PV–EC devices is the quickly changing landscape of silicon as a PV material. In the past 7 y, the price of crystalline silicon (c-Si) solar cells has decreased by 86%, and the price of PV modules has dropped 77%. In the meantime, average commercial c-Si solar-cell efficiencies have increased to 17.5% for multicrystalline silicon and 19.5% for monocrystalline silicon (50, 51). We now report an approach that leverages c-Si solar cells and our nonprecious metal catalysts to furnish a solar-to-fuels device with an efficiency of 10%. Because a single c-Si solar cell is unable to provide enough voltage to drive the water-splitting reaction, we use multiple single-junction solar cells series connected into minimodules. Although this approach does not result in a monolithic structure in which catalysts are directly deposited on the PV device in a buried-junction configuration (e.g., an artificial leaf), the equivalent circuit for both constructs is identical (52). This approach allows for modular independent optimization, after which the components could be integrated into a monolithic design. Our device bears resemblance to recently reported copper indium gallium diselenide-based devices (53), but incorporates low-cost and nonprecious crystalline silicon solar cells and oxygen-evolution and hydrogen-evolution catalysts.

Significance

For solar water splitting to be an economically viable resource, a 10% or higher solar-to-fuel conversion efficiency is required. Silicon photovoltaics (PV) are particularly attractive because silicon absorbs most of the solar spectrum, is nonprecious, and PV devices have dropped in price dramatically within the last decade. We demonstrate that by coupling a buried-junction silicon PV module with water-splitting catalysts, a 10% solar-to-fuels efficiency is achieved using all nonprecious and technology-ready materials.

Author contributions: C.R.C., J.Z.L., D.G.N., and T.B. designed research; C.R.C. and J.Z.L. performed research; C.R.C. contributed new reagents/analytic tools; C.R.C., J.Z.L., D.G.N., and T.B. analyzed data; and C.R.C., D.G.N., and T.B. wrote the paper.

The authors declare no conflict of interest.

Freely available online through the PNAS open access option.

[1]To whom correspondence may be addressed. Email: dnocera@fas.harvard.edu, buonassisi@mit.edu, or casandracox@fas.harvard.edu.

This article contains supporting information online at www.pnas.org/lookup/suppl/doi:10.1073/pnas.1414290111/-/DCSupplemental.

Results and Discussion

Fig. 1*A* shows a schematic of the coupled PV–EC device using a c-Si PV module, NiB_i as the oxygen-evolution catalyst (OEC) and NiMoZn as the hydrogen-evolution catalyst (HEC). By connecting the OEC to the *p*-type terminal and the HEC to the *n*-type terminal of the PV module, the voltage and current of the PV–EC system are constrained to be equal (Fig. 1*B*). This is true regardless of the mode for implementation (i.e., through wires or by directly depositing catalyst films on PV materials).

Because the PV–EC modular configuration allows independent optimization of the PV component and the electrochemical components, the operating point for a PV–EC device can be illustrated graphically as the intersection point of the independently measured *J–V* curves for the PV and EC for water splitting. The point of intersection gives the operation current density, J_{OP}, which is related to an SFE by multiplying by the thermodynamic potential for water splitting (1.23 V) and the Faradaic efficiency, η_{Far}:

$$\mathrm{SFE} = \frac{(1.23\mathrm{V}) \cdot J_{OP} \cdot \eta_{Far}}{P_{sun}\,(\mathrm{mW\ cm^{-2}})}. \quad [1]$$

The actual voltage required to drive the EC reaction is greater than the useful potential stored in the fuel (1.23 V), and is given by:

$$V_{EC} = 1.23\mathrm{V} + \eta_{OER} + \eta_{HER} + \eta_R, \quad [2]$$

where 1.23 V is the thermodynamic potential for water splitting, η_{OER} and η_{HER} are the overpotentials required for both half reactions (given by the Tafel behavior of the OER and HER catalysts), and η_R represents any additional resistive losses, such as contact resistance, resistance through electrodes, and solution resistance.

For maximum SFE, the intersection of the PV and EC current-voltage (*J–V*) curves occurs at a voltage equal to or greater than the voltage required for water splitting (Eq. **2**), but below the voltage at the maximum-power point of the PV module, V_{MPP}. This latter point is supported by Eq. **1**, whereby the efficiency is proportional to J_{OP}, which is maximized at voltages below V_{MPP}, as shown in Fig. 1. Fig. 1*C* shows the *J–V* curve for minimodules constructed from either three or four single-junction c-Si solar cells connected in series. When connecting the cells in series, the voltages are additive, and the current density decreases as 1/area (see *SI Appendix*, Table S1 for PV-module characteristics). We note that the overall PV efficiency is maintained upon connecting N cells in series because the module voltage will be xN larger than an individual cell, and the current density will be x1/N that of an individual cell.

Considering a PV–EC device based on commercially available single-junction Si solar cells and literature values for the previously reported Tafel behavior of the catalysts used herein (38, 44), equivalent-circuit modeling predicts a 10% or higher SFE can be achieved using three single-junction c-Si devices series connected in a minimodule with a PV efficiency of 15% or higher (red dashed curve in Fig. 1*C*). However, this is only the case if all resistive losses are negligible; if resistive losses are present, the operating point can occur to the right of V_{MPP}, reducing J_{OP} and SFE. Modeling indicates that using a four-cell c-Si module overcomes the impact of resistive losses on SFE (52).

To test these predictions, the steady-state current-voltage characteristics of the NiB_i anode and NiMoZn cathode were measured in a two-electrode setup in KB_i buffer at pH 9.2. The intersection at which the overlaid current-voltage characteristics of the half-reactions with the *J–V* curve of the PV minimodules illustrates J_{OP} and the resulting SFE for the coupled PV–EC device. Confirming the design considerations for resistive losses, we estimate an SFE of 2.8% for a three-cell module and 10% for a four-cell module (Fig. 1*C*).

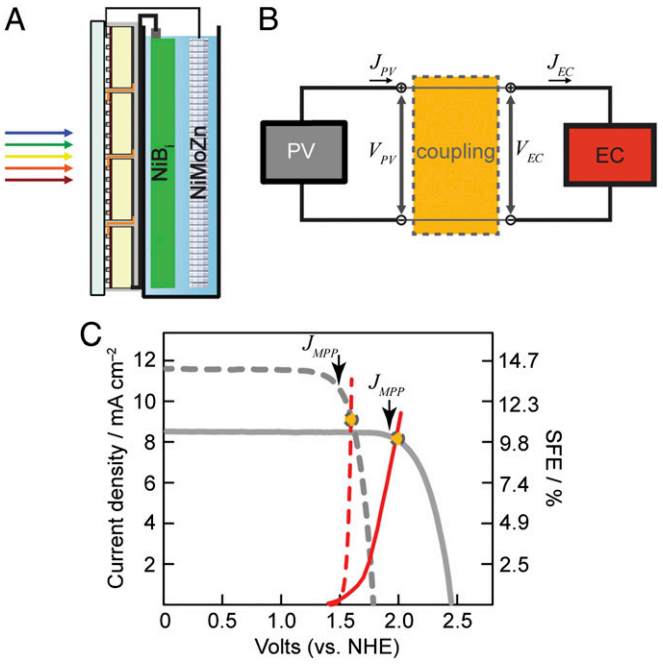

Fig. 1. (*A*) Schematic of the experimental setup and electrode geometry for the PV–EC device. (*B*) Block diagram for an electrochemical load driven by a PV device. The direct electrical connection in which the two half-reactions occur on surfaces equipotential with the terminals of a solar cell describes both wired and wireless water splitting and constrains the currents and voltages of the PV device and the EC system to be identical. (*C*) *J–V* curves of the individually measured PV and EC components making up the PV–EC device. The gray curves represent the *J–V* curve for the PV modules composed of either three (dashed) or four (solid) single junction c-Si solar cells measured under AM 1.5 illumination. The red dashed curve shows the ideal *J–V* curve obtained for NiB_i and NiMoZn catalysts based on previously reported Tafel analysis. The solid red curve curves show the *J–V* curve of the NiB_i and NiMoZn electrodes measured in a two-electrode experiment (0.5 M KB_i / 0.5 M K_2SO_4, pH 9.2). The point of intersection represents the J_{OP} and the SFE of the coupled system.

The simplest way to integrate the PV and EC components and verify the independently estimated SFE is to connect the PV module with the NiB_i anode and NiMoZn cathode. The photocurrent through the integrated device can be measured and should match the predicted J_{OP} obtained in Fig. 1*C*. The key criteria used to validate the SFE for a PV–EC device are the reporting protocols established by Chen et al. (54). These protocols include measurements using a two-electrode setup without the influence of an external potential bias, product quantification, and assessment of the long-term stability of the device under AM 1.5 illumination. In addition to product quantification, we wished to ensure that there was no parasitic current on J_{OP} due to product crossover reactions. Estimates of the maximum current for H_2 oxidation at the anode (*SI Appendix*) predict that a current density of 8.13 mA cm^{-2} (10% SFE) would have a parasitic current of 0.15 mA cm^{-2} (reducing 10.0% SFE to 9.8% SFE). However, the NiB_i is a specific OER catalyst. *SI Appendix*, Fig. S1 shows that the steady-state current density of the catalyst under Ar and H_2 is identical, indicating that this crossover reaction is negligible.

Fig. 2*A* shows the measured J_{OP} of the PV–EC device, which initially starts at 8.35 mA cm^{-2} corresponding to an SFE of 10.2%. During the first few minutes of illumination J_{OP} decreases to a steady-state value of 7.8 mA cm^{-2}. The initial decline in J_{OP} is consistent with heating of the PV module under illumination causing a decrease in solar cell voltage, which shifts the maximum power point toward the origin. This is confirmed

by measuring the V_{OC} of the minimodule as a function of time showing a ~130 mV decrease, which is consistent in a temperature change of 15 °C (*SI Appendix*, Fig. S2) (55). In line with PV module heating, turning the lamp off for 5 min and then turning it back on causes the SFE to recover to 10.2% (Fig. 2*A*). Additionally, the chopped illumination demonstrates good reproducibility in measuring J_{OP}.

The largest efficiency losses for the PV–EC device result from series resistance through the electrodes (R_{EL}) and solution resistance (R_{SOL}). The former is straightforward to address by using metal electrodes as substrates for the OER and HER catalysts making contact resistance and resistance through the electrodes negligible. Solution resistance in buffered electrolytes, as opposed to strong acids or bases, remains a challenge. The primary reason for a less than optimal R_{SOL} is the limited solubility of the buffer (56). In the case of borate buffer, this is the solubility limit of boric acid, which is ~1 M corresponding to a specific conductance of 26 mS cm^{-1}. The specific conductivity can be improved by adding an inert salt as a supporting electrolyte (*SI Appendix*, Fig. S3). For example, when using KNO_3, the specific conductance of 0.5 M KB_i / 1.5 M KNO_3 is 126 mS cm^{-1}.

The choice of supporting electrolyte is rather straightforward in typical electrochemical experiments where only one half-reaction at either the anode or cathode is of interest. When considering deleterious side reactions for both the anode and cathode, the supporting electrolyte must be inert over a wider potential range. Given our modular approach, the choice of supporting electrolyte was determined by measuring the Faradaic efficiency for each electrode/electrolyte configuration independently before being implemented into the PV–EC device. For example, when operating the NiMoZn cathode for HER at current densities of 10 mA cm^{-2}, GC analysis showed no hydrogen production, indicating that NO_3^- is preferentially reduced as opposed to protons. Alternatively, using K_2SO_4 as a supporting electrolyte results in a Faradaic efficiency of 100% (Fig. 2*C*). However, K_2SO_4 is sparingly soluble at 0.5 M, once again limiting the specific conductivity of our electrolyte to 90 mS cm^{-1} (*SI Appendix*, Fig. S3). By moving to a more conductive electrolyte, such as 1 M KOH (pH 14), an initial SFE greater than 12% can be obtained with a three-cell minimodule as opposed to a four-cell module (*SI Appendix*, Fig. S4). This also shows how minimizing R_{SOL} shifts the EC curve closer to the ideal curve obtained based on the Tafel analysis of the catalysts used herein (*SI Appendix*, Fig. S5). However, we prefer to avoid the deleterious effect of concentrated base on PV materials by staying in neutral and near-neutral conditions. The purported challenges arising from R_{SOL} in nonbasic conditions as derived from simple modeling (57) may be overcome by using clever flow-cell designs, which also introduce mechanisms of gas separation and collection, as well as optimized cell geometries (58, 59). We also note that to avoid gas mixing in this device, a membrane will be needed between oxygen evolution and hydrogen-evolution catalysts.

The operational stability of the coupled PV–EC system showed no decline in J_{OP} for over a week of operation in 0.5 M KB_i pH 9.2 solution. Interestingly, the SFE, inferred from the current, appears to slightly increase during the first 24 h of operation. We attribute this to a small recovery in cell voltage over the course of 24 h of illumination (blue line in *SI Appendix*, Fig. S2). Initially, the module absorbs heat from the solar simulator photon flux, causing the initial decrease in PV efficiency (60). Then, under constant illumination at higher temperatures, the observation of a gradual improvement in the current density over a timescale of tens of hours is consistent with the evolution of the "oxygen–boron defect," a well-studied phenomenon in *p*-type Czochralski silicon (61). It is important to note that the observed fluctuations in J_{OP} and SFE are direct manifestations of fluctuations in the PV-module output and are not related to the PV–EC coupling or EC reactions.

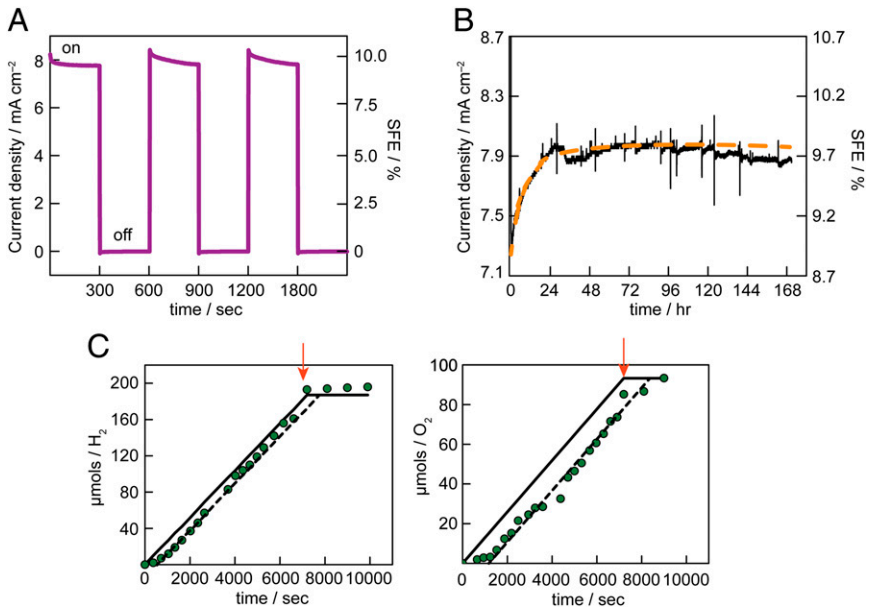

Fig. 2. (*A*) Current under chopped illumination representing J_{OP} for the PV–EC device (0.5 M KB_i / 0.5 M K_2SO_4, pH 9.2). The chopped illumination illustrates the recovery in SFE and illustrates the reproducibility in measuring J_{OP}. (*B*) J_{OP} measured for over 7 d of operation showing no decrease in SFE over operation time. Spikes in J_{OP} are due to addition of solution to maintain the solution level and pH. The orange dashed line is a smoothed curve of the data. (*C*) Gas quantification for the NiMoZn cathode and NiB_i anode in 0.5 M KB_i / 0.5 M K_2SO_4 pH 9.2 solution. The black lines represent 100% Faradaic efficiency based on the charge passed during electrolysis. The green circles represent the H_2 and O_2 measured by gas chromatography. Red arrows indicate when electrolysis was stopped. GC analysis was conducted until the moles of gas measured in the headspace reached a steady state. The lag period in gas generation is due to the buildup of gases in the head space of the EC cell.

Conclusion

We demonstrate that an SFE efficiency of 10% can be achieved using nonprecious materials and c-Si. This proof of concept capitalizes on the declining cost of high-quality PV devices and earth-abundant catalysts operating under near-neutral-pH conditions. This modular design of the PV and EC components allows for a wide variety of PVs materials, catalysts, and electrolytes to be implemented where no one component is constrained by the other. This methodology permits facile optimization and characterization. As PV–EC device subcomponents reach technological maturity, an increasing emphasis will be placed on system design and integration, which will allow for larger scalability, specifically future designs that incorporate mechanisms gas separation and collection as well, minimization of resistive losses through flow cells designs, and optimization of cell geometries.

Experimental

Materials and Methods. Nickel (II) chloride hexahydrate, boric acid, potassium hydroxide, potassium nitrate, and potassium sulfate were purchased from Sigma Aldrich and used as received. Steel foil and nickel mesh were purchased from Strem. Crystalline silicon minimodules were made from single-junction commercial cells fabricated from Czochralski silicon with stand-alone efficiencies of 18%. After laser cutting the commercial cells, connecting four in series, and encapsulating them with ethylene vinyl acetate, the minimodule efficiency was 16%. The equivalent minimodule for a three-cell series is 15.8%. Additional details concerning laser cutting and module encapsulation are provided in the *SI Appendix*.

Electrochemical experiments were performed using a CH-Instruments 760D potentiostat. For three-electrode measurements, potentials were measured against an Ag/AgCl reference electrode (BASi) and converted to normal hydrogen electrode by adding 0.197 V. For two electrode experiments, the working electrode lead of the potentiostat was connected to the anode and the reference and auxiliary leads of the potentiostat were connected to the cathode.

The NiB_i anode was electrodeposited in a two-compartment electrochemical cell with a glass frit junction. The working compartment was charged with ∼25 mL of 0.2 M B_i electrolyte and 25 mL of a 1 mM Ni^{2+} solution. The working electrode was a steel substrate, and the NiB_i catalyst was deposited by applying a voltage of 0.95 V (vs. Ag/AgCl) for 1 h. To improve anode activity the electrodes were then anodized at 0.9 V (vs. Ag/AgCl) in 1 M KOH for 1 h (31).

The NiMoZn cathode was electrodeposited from a solution of nickel(II) chloride hexahydrate (9.51 g L^{-1}), sodium molybdate dihydrate (4.84 g L^{-1}), anhydrous zinc chloride (0.0409 g L^{-1}), tetrabasic sodium pyrophosphate (34.57 g L^{-1}), and sodium bicarbonate (74.77 g L^{-1}; VWR). Hydrazine hydrate (1.21 mL L^{-1}; Alfa Aesar) was added immediately before plating. NiMoZn was deposited onto a Ni mesh substrate that had been pretreated at –2 V vs. Ag/AgCl in 0.5 M H_2SO_4 for 3 min. The NiMoZn alloy was deposited at a voltage of –1.8 V (vs. Ag/AgCl) for 30 min. The deposit was left to dealloy overnight in 6 M KOH (43).

The NiB_i anode and NiMoZn cathode were connected in series with the c-Si minimodule. The light source was a Sol 2A solar simulator (Newport Corp.). The current through the PV–EC device was measured by using the potentiostat as an ammeter. The electrodes operated in a small beaker with ∼60 mL of solution and ∼1 cm distance between the anode and cathode. For all measurements no stirring was involved as it requires an additional energy input and would have to be factored into the SFE. In all cases, the area used to convert current to current density was the active area of the c-Si minimodule. In addition, the geometric area of the anode and cathode was scaled to match that of the minimodule. For long-term stability measurements, ∼1 mL of solution was added per day to compensate for evaporation. Additionally, the pH of solution was measured periodically and showed no change.

The Faradaic efficiency for each electrode was evaluated using gas chromatography. The experiment was performed galvanostatically using a three-electrode configuration in a custom built two-compartment gas-tight electrochemical cell. The working electrode was either NiB_i on a steel substrate for O_2 quantification, or NiMoZn on a nickel mesh substrate for H_2 quantification. The working electrode operated at a constant current density of 10 mA cm^{-2} for 2 h. During the course of the experiment, samples of evolved gas were removed from the headspace and injected into the GC. To ensure that the evolved gas reached a steady-state value in the headspace, GC measurements were recorded for 1 h after cessation of electrolysis. The data were converted into partial pressure of gas in the headspace using calibration curves defined from known mixtures of H_2/N_2 or O_2/N_2. The partial pressure of gas was converted to μmol, and corrected using Henry's law to account for the gas dissolved in solution. The total charge passed during electrolysis was divided by *n*F (*n* corresponding to the number of electrons in each half reaction) to furnish the calculated gas yield. The total calculated and experimental gas yields were used to determine the Faradaic efficiency.

The influence of H_2 on the steady-state activity of the NiB_i OER catalyst was evaluated galvanostatically in a three-electrode setup (0.5 M KB_i / 0.5 M K_2SO_4 pH 9.2). Steady-state current voltage was collected first by saturating the continuous bubbling of Ar throughout the working-electrode compartment, and then by repeating the measurement in H_2 saturated solution with continuous bubbling during the course of the experiment.

ACKNOWLEDGMENTS. The authors acknowledge helpful discussions with Joseph T. Sullivan (Massachusetts Institute of Technology), Kwabena Bediako (Harvard University), and Tom Kempa (Harvard University). This work was supported through National Science Foundation Faculty Early Career Development Program ECCS-1150878 (to T.B.), Air Force Office of Scientific Research Grant FA9550-13-1-0028 (to D.G.N.), the National Research Foundation Singapore through the Singapore Massachusetts Institute of Technology Alliance for Research and Technology's Low Energy Electronic Systems research program (T.B.), and a generous gift from the Chesonis Family Foundation.

1. Cook TR, et al. (2010) Solar energy supply and storage for the legacy and nonlegacy worlds. *Chem Rev* 110(11):6474–6502.
2. Lewis NS, Nocera DG (2006) Powering the planet: Chemical challenges in solar energy utilization. *Proc Natl Acad Sci USA* 103(43):15729–15735.
3. Crabtree GW, Dresselhaus MS (2008) The hydrogen fuel alternative. *MRS Bull* 33:421–428.
4. Vielstch W, Lamm A, Gasteiger HA, eds (2003) *Handbook of Fuel Cells: Fundamentals, Technology and Applications* (John Wiley, Chichester, UK).
5. Li CW, Ciston J, Kanan MW (2014) Electroreduction of carbon monoxide to liquid fuel on oxide-derived nanocrystalline copper. *Nature* 508(7497):504–507.
6. Medina-Ramos J, DiMeglio JL, Rosenthal J (2014) Efficient reduction of CO_2 to CO with high current density using in situ or ex situ prepared Bi-based materials. *J Am Chem Soc* 136(23):8361–8367.
7. Smieja JM, et al. (2013) Manganese as a substitute for rhenium in CO_2 reduction catalysts: The importance of acids. *Inorg Chem* 52(5):2484–2491.
8. Khaselev O, Bansal A, Turner JA (2001) High-efficiency integrated multijunction photovoltaic/electrolysis systems for hydrogen production. *Int J Hydrogen Energy* 26:127–132.
9. US Department of Energy (2013) Hydrogen, fuel cells, & infrastructure technologies program. Hydrogen production. Available at http://www1.eere.energy.gov/hydrogenandfuelcells/mypp/. Accessed April 30, 2014.
10. Walter MG, et al. (2010) Solar water splitting cells. *Chem Rev* 110(11):6446–6473.
11. Osterloh FE (2008) Inorganic materials as catalysts for photochemical splitting of water. *Chem Mater* 20:35–54.
12. Lin F, Boettcher SW (2014) Adaptive semiconductor/electrocatalyst junctions in water-splitting photoanodes. *Nat Mater* 13(1):81–86.
13. Mills TJ, Lin F, Boettcher SW (2014) Theory and simulations of electrocatalyst-coated semiconductor electrodes for solar water splitting. *Phys Rev Lett* 112(14): 148304–148305.
14. Weber MF, Dignam MJ (1986) Splitting water with semiconducting photoelectrodes-Efficiency considerations. *Int J Hydrogen Energy* 11:225–232.
15. Weber MF, Dignam MJ (1984) Efficiency of splitting water with semiconducting photoelectrodes. *J Electrochem Soc* 131:1258–1265.
16. Bolton JR, Strickler SJ, Connolly JS (1985) Limiting and realizable efficiencies of solar photolysis of water. *Nature* 316:495–500.
17. Cukier RI, Nocera DG (1998) Proton-coupled electron transfer. *Annu Rev Phys Chem* 49:337–369.
18. Eisenberg R, Gray HB (2008) Preface on making oxygen. *Inorg Chem* 47(6):1697–1699.
19. Betley TA, Wu Q, Van Voorhis T, Nocera DG (2008) Electronic design criteria for O-O bond formation via metal-oxo complexes. *Inorg Chem* 47(6):1849–1861.
20. Betley TA, et al. (2008) A ligand field chemistry of oxygen generation by the oxygen-evolving complex and synthetic active sites. *Philos Trans R Soc Lond B Biol Sci* 363(1494):1293–1303, discussion 1303.
21. Hammes-Schiffer S (2009) Theory of proton-coupled electron transfer in energy conversion processes. *Acc Chem Res* 42(12):1881–1889.
22. Concepcion JJ, et al. (2009) Making oxygen with ruthenium complexes. *Acc Chem Res* 42(12):1954–1965.
23. Khaselev O, Turner JA (1998) A monolithic photovoltaic-photoelectrochemical device for hydrogen production via water splitting. *Science* 280(5362):425–427.
24. Miller EL, Rocheleau RE, Deng XM (2003) Design considerations for a hybrid amorphous silicon/photoelectrochemical multijunction cell for hydrogen production. *Int J Hydrogen Energy* 28:615–623.

25. Rocheleau RE, Miller EL, Misra A (1998) High–efficiency photoelectrochemical hydrogen production using multijunction amorphous silicon photoelectrodes. *Energy Fuels* 12:3–10.
26. Hanna MC, Nozik AJ (2006) Solar conversion efficiency of photovoltaic and photoelectrolysis cells with carrier multiplication absorbers. *J Appl Phys* 100:074510/1–8.
27. Rocheleau RE, Miller EL (1997) Photoelectrochemical production of hydrogen: Engineering loss analysis. *Int J Hydrogen Energy* 22:771–782.
28. Bard AJ, Fox MA (1995) Artificial photosynthesis: Solar splitting of water to hydrogen and oxygen. *Acc Chem Res* 28:141–145.
29. Kanan MW, Nocera DG (2008) In situ formation of an oxygen-evolving catalyst in neutral water containing phosphate and Co^{2+}. *Science* 321(5892):1072–1075.
30. Surendranath Y, Dincă M, Nocera DG (2009) Electrolyte-dependent electrosynthesis and activity of cobalt-based water oxidation catalysts. *J Am Chem Soc* 131(7):2615–2620.
31. Lutterman DA, Surendranath Y, Nocera DG (2009) A self-healing oxygen-evolving catalyst. *J Am Chem Soc* 131(11):3838–3839.
32. Kanan MW, et al. (2010) Structure and valency of a cobalt-phosphate water oxidation catalyst determined by in situ X-ray spectroscopy. *J Am Chem Soc* 132(39): 13692–13701.
33. Surendranath Y, Kanan MW, Nocera DG (2010) Mechanistic studies of the oxygen evolution reaction by a cobalt-phosphate catalyst at neutral pH. *J Am Chem Soc* 132(46):16501–16509.
34. Surendranath Y, Lutterman DA, Liu Y, Nocera DG (2012) Nucleation, growth, and repair of a cobalt-based oxygen evolving catalyst. *J Am Chem Soc* 134(14):6326–6336.
35. Farrow CL, Bediako DK, Surendranath Y, Nocera DG, Billinge SJL (2013) Intermediate-range structure of self-assembled cobalt-based oxygen-evolving catalyst. *J Am Chem Soc* 135(17):6403–6406.
36. Liu Y, Nocera DG Spectroscopic studies of nanoparticulate thin films of a cobalt-based oxygen evolution catalyst. *J Phys Chem C*, 10.1021/jp5008347.
37. Dincă M, Surendranath Y, Nocera DG (2010) Nickel-borate oxygen-evolving catalyst that functions under benign conditions. *Proc Natl Acad Sci USA* 107(23):10337–10341.
38. Bediako DK, et al. (2012) Structure-activity correlations in a nickel-borate oxygen evolution catalyst. *J Am Chem Soc* 134(15):6801–6809.
39. Bediako DK, Surendranath Y, Nocera DG (2013) Mechanistic studies of the oxygen evolution reaction mediated by a nickel-borate thin film electrocatalyst. *J Am Chem Soc* 135(9):3662–3674.
40. Huynh M, Bediako DK, Liu Y, Nocera DG (2014) Nucleation and growth mechanisms of an electrodeposited manganese oxide catalyst at near-neutral pH. *J Phys Chem C*, 10.1021/jp501768n.
41. Huynh M, Bediako DK, Nocera DG (2014) A functionally stable manganese oxide oxygen evolution catalyst in acid. *J Am Chem Soc* 136(16):6002–6010.
42. Reece SY, et al. (2011) Wireless solar water splitting using silicon-based semiconductors and earth-abundant catalysts. *Science* 334(6056):645–648.
43. Pijpers JJH, Winkler MT, Surendranath Y, Buonassisi T, Nocera DG (2011) Light-induced water oxidation at silicon electrodes functionalized with a cobalt oxygen-evolving catalyst. *Proc Natl Acad Sci USA* 108(25):10056–10061.
44. Cox CR, Winkler MT, Pijpers JJH, Buonassisi T, Nocera DG (2012) Interfaces between water splitting catalysts and buried silicon junctions. *Energy Environ Sci* 6:532–538.
45. Young ER, Costi R, Paydavosi S, Nocera DG, Bulović V (2011) Photo-assisted water oxidation with cobalt-based catalyst formed from thin-film cobalt metal on silicon photoanodes. *Energy Environ Sci* 4:2058–2061.
46. Costi R, Young ER, Bulović V, Nocera DG (2013) Stabilized CdSe-CoPi composite photoanode for light-assisted water oxidation by transformation of a CdSe/cobalt metal thin film. *ACS Appl Mater Interfaces* 5(7):2364–2367.
47. Nocera DG (2012) The artificial leaf. *Acc Chem Res* 45(5):767–776.
48. Cristino V, et al. (2013) Efficient solar water oxidation using photovoltaic devices functionalized with earth-abundant oxygen evolving catalysts. *Phys Chem Chem Phys* 15(31):13083–13092.
49. Hu S, et al. (2014) Amorphous TiO_2 coatings stabilize Si, GaAs, and GaP photoanodes for efficient water oxidation. *Science* 344(6187):1005–1009.
50. Powell DM, et al. (2012) Crystalline silicon photovoltaics: A cost analysis framework for determining technology pathways to reach baseload electricity costs. *Energy Environ Sci* 5:5874–5883.
51. Chu S, Majumdar A (2012) Opportunities and challenges for a sustainable energy future. *Nature* 488(7411):294–303.
52. Winkler MT, Cox CR, Nocera DG, Buonassisi T (2013) Modeling integrated photovoltaic–electrochemical devices using steady-state equivalent circuits. *Proc Natl Acad Sci USA* 110:E1076–E1082.
53. Jacobsson TJ, Fjällström V, Sahlberg M, Edoff M, Edvinsson T (2013) A monolithic device for solar water splitting based on series interconnected thin film absorbers reaching over 10% solar-to-hydrogen efficiency. *Energy Environ Sci* 6:3676–3683.
54. Chen Z, et al. (2010) Accelerating materials development for photoelectrochemical hydrogen production: Standards for methods, definitions, and reporting protocols. *J Mater Res* 25:3–16.
55. Fan JCC (1986) Theoretical temperature dependence of solar cell parameters. *Solar Cells* 17:309–315.
56. Hernández-Pagán EA, et al. (2012) Resistance and polarization losses in aqueous buffer–membrane electrolytes for water-splitting photoelectrochemical cells. *Energy Environ Sci* 5:7582–7589.
57. Jin J, Walczak K, Karp C, Lewis NS, Xiang C (2014) An experimental and modeling/simulation-based evaluation of the efficiency and operational performance characteristics of an integrated, membrane-free, neutral pH solar-driven water-splitting system. *Energy Environ Sci* 7:3371–3380.
58. Haussener S, et al. (2012) Modeling, simulation, and design criteria for photelectrochemical water-splitting systems. *Energy Environ Sci* 5:9922–9935.
59. Modestino MA, et al. (2013) Robust production of purified H2 in a stable, self-regulating, and continuously operating solar-fuel generator. *Energy Environ Sci* 7:297–301.
60. Jones AD, Underwood CP (2001) Thermal model for photovoltaic systems. *Sol Energy* 70:349–359.
61. Bianca L, Karsten B, Schmidt J (2008) Deactivation of the boron-oxygen recombination center in silicon by illumination at elevated temperature. *Phys Status Solidi Rapid Res Lett* 2:93–95.